Tribol Lett (2013) 49:193–202
DOI 10.1007/s11249-012-0057-y

ORIGINAL PAPER

# Dry Friction Between Laser-Patterned Surfaces: Role of Alignment, Structural Wavelength and Surface Chemistry

**Carsten Gachot · Andreas Rosenkranz · Leander Reinert · Estéban Ramos-Moore · Nicolas Souza · Martin H. Müser · Frank Mücklich**

Received: 27 July 2012 / Accepted: 3 October 2012 / Published online: 17 November 2012


**Abstract** The ability to tune friction by tailoring surface topographies at micron length scales and by changing the relative orientation of crystallites at the atomic scale is well established. Here, we investigate if the two concepts combine, i.e. if the relative orientation of surfaces affects dry friction between laser-textured surfaces. Laser patterning was used on austenitic stainless steel substrates and on tribometer testing balls made of 100Cr6 to create linear periodic arrays with different structural wavelengths or periodicities (5, 9 and 18 μm). Pairing each substrate with a ball of the same periodicity, the different arrays were subjected to dry sliding tests at 0°/90° relative alignment between the linear patters. We observe that the patterning reduces friction after running-in. The reduction increases with decreasing wavelength and also depends sensitively on the relative alignment and the chemistry of the sliding surfaces. Our results highlight the possibility to create tailored contacting surface geometries leading to tunable frictional properties.

**Keywords** Laser interference patterning · Dry friction · Interlocking

C. Gachot (✉) · A. Rosenkranz · L. Reinert · E. Ramos-Moore · N. Souza · F. Mücklich
Department of Materials Science and Engineering, Saarland University, Campus, 66123 Saarbrücken, Germany
e-mail: c.gachot@mx.uni-saarland.de

E. Ramos-Moore
Facultad de Fisica, Pontificia Universidad Catolica de Chile, 7820436 Santiago, Chile

M. H. Müser
Jülich Supercomputing Centre, Wilhelm-Johnen Str., 52425 Jülich, Germany

## 1 Introduction

Most machines contain components with loaded solid surfaces that rub together. The interaction of such surfaces produces friction and also results in mechanical damage to them. Thus, tribological phenomena play a decisive role in diverse systems. For many years, researchers have sought to alleviate these problems and to understand their origin. The early work of Bowden and Tabor [1] showed that one influential aspect on friction is the interaction of asperities. They can be welded together and released by applying a critical shear stress $\tau_c$. However, studies at different spatial scales revealed that tremendously small shear stresses between atomically flat surfaces are possible when their surface corrugation does not match [2]. Such a state of nearly vanishing friction was introduced by the pioneering work of Hirano and Shinjo [2] for incommensurate, i.e. non-matching contacts, and confirmed experimentally by Dienwiebel et al. [3] on the nanometre scale. Recently, Sondhauß et al. have demonstrated the influence of a mesoscopically patterned silicon surface on the frictional response. They used a silicon substrate which was patterned using a focused ion beam microscope (FIB) and, as a counterbody, titanium spheres (without pattern) with different radii attached to a slightly modified AFM cantilever. It was shown that the effective coefficient of friction has characteristic maxima depending on the groove widths in the silicon substrate and the corresponding radius of the titanium spheres [4].

The ability to control and modify frictional forces on different scales bears promise for the design of miniaturised systems, positioning devices and bearings [5]. There are two major methods to manipulate friction: modification of the surface materials or texturing of the relevant surfaces [6, 7]. In particular, laser surface texturing (LST),

introduced by the Etzion group for the texturing of mechanical seals, proved to be a promising technique for dry and lubricated contacts [8–11].

One possible approach to LST is laser interference metallurgy. It is based on the interference of laser beams from a solid-state laser, which creates well-defined surface topographies on the micron scale [12–15]. Moreover, due to a periodic laser intensity distribution and significant heating/cooling rates of up to $10^{10}$ K/s [16], metallurgical effects like melting, resolidification and the formation of intermetallic phases can be induced [17, 18]. In the present work, we apply the aforementioned technique to pattern both interacting surfaces, rather than just one, to control the involved contact geometries under dry sliding conditions. Using two-beam interference, linear patterns with varying periodicity of the laser intensity maxima were fabricated. Furthermore, the as-patterned contacting bodies were scrutinised with regard to their ability to interlock depending on the structural wavelength and the relative alignment. In addition, microstructural (X-ray diffraction) and chemical analysis (Raman spectroscopy) were applied to study the laser-treated specimens. Finally, experimental results of the frictional response will be presented and discussed.

## 2 Experimental Procedure

A commercially available austenitic stainless steel (1.4301) was used for the laser experiments. The lateral dimensions of the nominally flat specimens are $20 \times 20$ mm$^2$. The samples were delivered with a highly polished mirror-like surface finish having a root mean square roughness of about 30 nm. A pulsed Nd: YAG laser (Spectra Physics, Quanta Ray PRO 290) with a pulse duration of 10 ns was used for the laser structuring. The primary laser beam was split into two sub-beams to interfere with each other on the sample surface resulting in a line-like interference pattern (Fig. 1).

The intensity of each beam can be controlled using suitable beam splitters. The laser fluence was set to 400 mJ/cm$^2$ for all specimens. Due to the absorption characteristics of the material used, the third harmonic at 355 nm was selected. The periodicity (line-spacing) was set to be about 5, 9 and 18 μm. All samples were irradiated

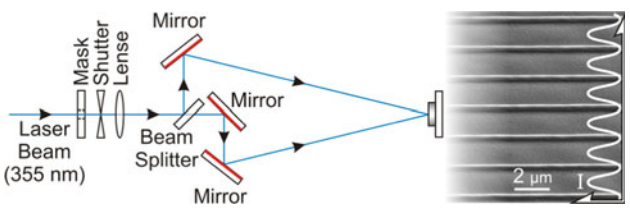


**Fig. 1** Schematic diagram of the interference setup. The SEM image shows a typical interference line-pattern made on stainless steel

at normal atmospheric conditions in air using one single laser pulse. Further details of the experimental setup have already been published elsewhere [13].

The topography was measured by a Zygo New View 100 white light interferometer (WLI) equipped with a 3-D imaging surface structure analyser.

The surface morphology was imaged by scanning electron microscopy (SEM) (FEI, Strata DB 235). In addition, a FIB microscope (FEI, Strata DB 235) was selected to prepare cross sections in order to investigate the microstructure.

XRD phase analysis measurements using grazing incidence geometry (GI-XRD) were carried out in order to obtain statistically relevant phase data of a significantly large specimen volume. For this purpose, a seven-axe diffractometer (PANalytical X'PERT MPD Pro) with a copper X-ray tube was used.

Raman spectroscopy was performed with a LabRAM ARAMIS instrument from HORIBA using a 532 nm laser beam without filter. The Raman microscope uses a backscattering geometry, where the incident beam is linearly polarised and the spectral detection is unpolarised. The optical elements used in this analysis allowed a laser spot size of 5 μm (full width at half maximum) and depth penetration of $\sim$1 μm, while the spectra precision was around 5 cm$^{-1}$.

The tribological tests were performed with a nanotribometer using a ball on disc configuration in a linear reciprocating sliding mode (CSM Instruments) with a stroke length of 0.6 mm. The tribometer is based on a stiff cantilever, which acts as a frictionless force transducer in both vertical and horizontal directions. The static partner is loaded onto the substrate with a precisely known force using piezo-actuation. The normal load and the friction force are determined during the experiment by measuring the deflection of this elastic arm in both horizontal and vertical planes with two high-precision fibre-optical displacement sensors. Through a feedback loop, the piezo-actuation maintains the normal load independent of any surface irregularities. The normal force was set to 1 mN and the linear sliding speed to 1 mm/s. The deviation of the aforementioned normal load was less than 10 % with respect to the reference value in our experiments. The counterbody consisted of a typical 100Cr6 bearing steel ball with a diameter of 3 mm. Temperature and relative humidity were kept constant at 20 ± 2 °C and 45 ± 5 %.

## 3 Results and Discussion

### 3.1 Topographical Analysis

Figure 2 shows a typical line-pattern on a stainless steel substrate with a structural wavelength of around 9 μm.

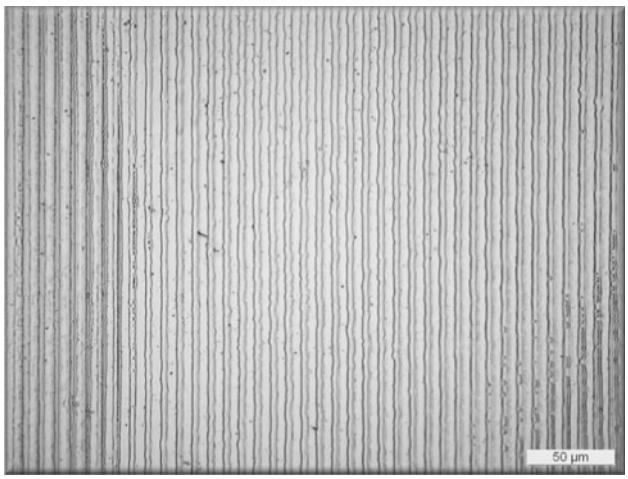


**Fig. 2** Two-beam interference line-pattern on a 1.4301 stainless steel substrate with a periodicity of around 9 µm measured by light microscopy

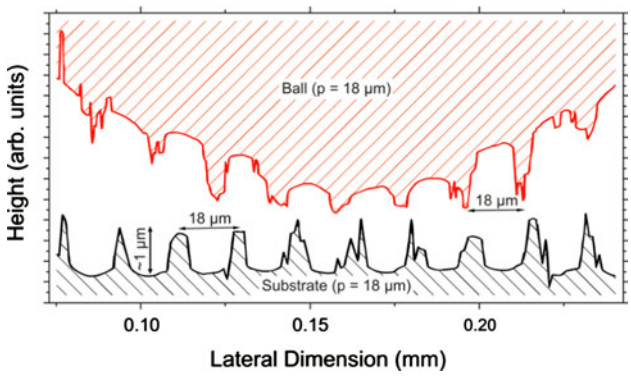


**Fig. 3** Topography plots for a patterned steel substrate (*black*) and a 100Cr6 tribometer ball (*red*) measured by WLI

The pattern, resulting from two interfering beams, is uniformly distributed and largely homogeneous.

The observed line-pattern is a result of a temperature gradient between positions of maximum and minimum laser intensity. It induces a surface tension gradient, which shifts molten material away from the hot regions. The shifted material resolidifies in the intensity minima. In addition to optical microscopy, WLI measurements were performed in order to analyse the topography of the resulting pattern on the substrate and ball surfaces (see Fig. 3).

For a geometrical interlocking of the two patterned surfaces, the groove and asperity widths of the contact surfaces are essential. Figure 3 shows cross section plots of a patterned steel substrate and tribometer ball measured by WLI. The laser periodicity in both cases was set to 18 µm with a depth of around 1 µm. The analysed groove widths of the profiles presented in Fig. 3 range from 12 to 14 µm in the upper part and from 7 to 9 µm in the lower part of the structured substrate. The asperity widths for both surfaces range between 3 and 10 µm. Therefore, an interlocking of the structures based upon the topographical analysis is generally possible.

Additionally, the line-patterns with varying periodicity were studied with regard to surface profile parameters and compared to each other.

The slope roughness $S_{RMS}$, the skewness $R_{sk}$, the kurtosis $R_{ku\psi}$ and the Swedish height $H$ were determined by WLI. In particular, the Swedish height represents the distance between two reference lines where the upper reference line covers 5 % of the data and the lower one 90 %. As a result, this value is less sensitive to surface artifacts such as spikes which may appear during WLI measurements [19]. Figure 4 depicts the surface profile plots for the three different periodicities. The height deviations for a line-spacing of 5 µm are more pronounced than for the other periodicities. When decreasing the periodicity, the lateral thermal flow becomes more important thus setting a lower physical limit, which is similar to the thermal diffusion length for most metals [20]. If laser patterns with periodicities in the range of the thermal diffusion length are created, the thermal gradient between the regions of maximum and minimum laser intensity will be reduced. Consequently, the specific metal will be molten in both positions. According to Lasagni et al. [20], the minimum achievable structural wavelength in stainless steel is about 1.3 µm. Table 1 summarises the mentioned surface parameters. The average values are based on ten measurements of the respective parameters. The RMS value of the reference sample is relatively low compared to the laser-patterned surfaces. This is due to the mirror-like surface finish of the specimens. The Swedish height $H$ shows a maximum value of around 1.6 µm for a periodicity of 18 µm. There is a direct correlation, already studied by Lasagni [21], between the structural depth and the structural wavelength used. Usually, this depth increases for larger structural wavelengths. This is attributed to the aforementioned thermal gradient, which is generally smaller for lower periodicities. Furthermore, the reference specimen has a negative skewness indicating good bearing properties. In contrast, all laser-patterned surfaces show positive values due to the reduced bearing capability. The highest positive value can be found for the sample with the largest structural wavelength.

Apart from the reference, the 9 µm pattern has the lowest positive $R_{sk\psi}$value. A comparison with the corresponding cross section profile plot reveals a very homogeneous laser-pattern. During the laser-induced melting process, the material is shifted away from the intensity maximum towards the minimum positions. In case of larger wavelengths, the distance between the maximum and minimum positions is expanded and so the distance in between cannot be bridged by the molten material.

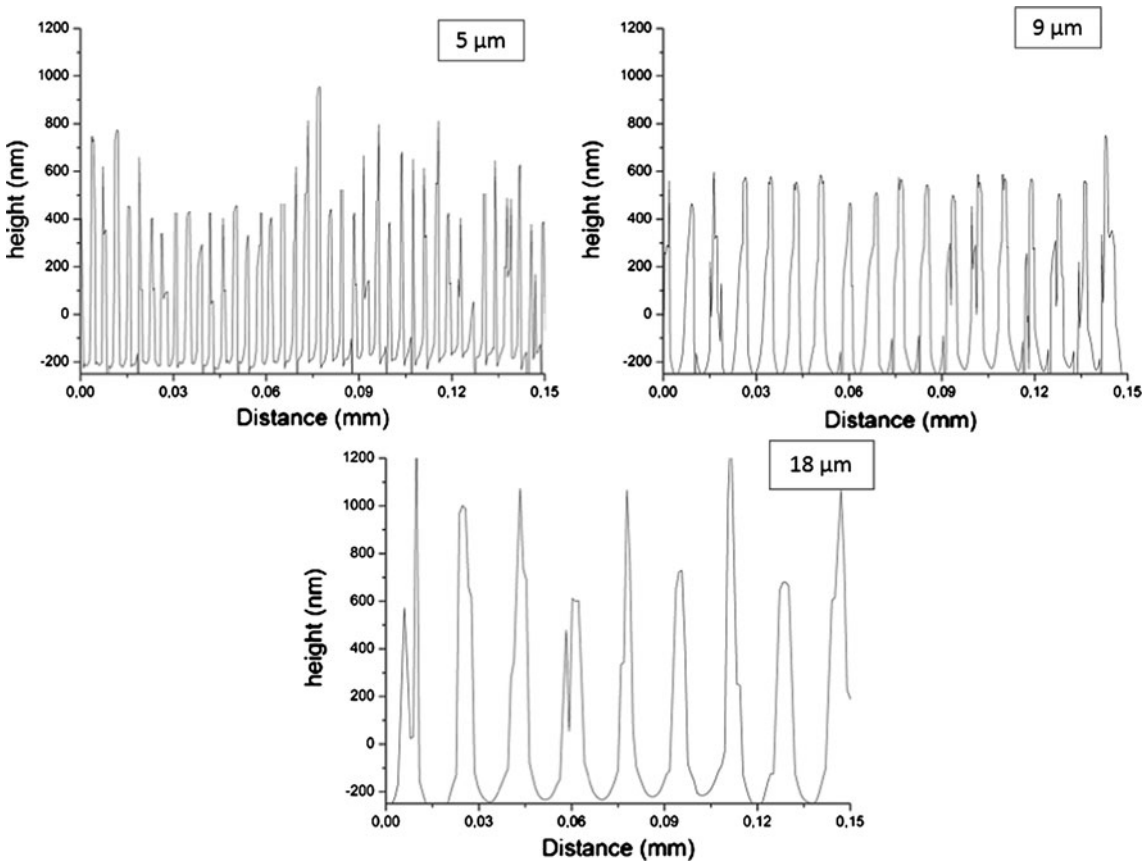


**Fig. 4** Surface profile plots of laser-patterned steel surfaces measured by WLI. The periodicity was set to be 5, 9 and 18 µm

**Table 1** Topographical parameters of laser-patterned samples in comparison with the unpatterned reference recorded by WL

| Parameter | RMS (nm) | $S_{RMS}$ (µm/mm) | $H$ (nm) | $R_{sk}$ | $R_{ku}$ |
|---|---|---|---|---|---|
| Unpatterned reference | 34 ± 5 | 26.32 ± 4 | 94.45 ± 11 | −1.5 ± 0.2 | 3.12 ± 0.8 |
| 5 µm | 326 ± 12 | 626.44 ± 57 | 860 ± 49 | 0.84 ± 0.03 | 3.59 ± 0.26 |
| 9 µm | 305 ± 6 | 484.89 ± 36 | 775 ± 11 | 0.52 ± 0.07 | 2.38 ± 0.19 |
| 18 µm | 354 ± 34 | 218.05 ± 15 | 1164 ± 107 | 1.45 ± 0.13 | 5.30 ± 0.53 |

As a consequence, additional topographical maxima may appear with different heights.

The slope RMS, $S_{RMS}$, is listed for the various specimens. This parameter is particularly interesting because it represents the square-root of the second order spectral moment, which can be found in literature as $(m_2)^{1/2}$, and is roughly inversely proportional to the real area of contact [22]. As expected for similar structure depths, $S_{RMS\psi}$ is the highest for the smaller structural wavelength.

### 3.2 Microstructural and Mechanical Characterisation

The pristine steel surface is shown in Fig. 5. Some polishing artifacts are still visible. Despite the polishing marks, a coarse-grained microstructure is revealed by using ion channelling contrast in a SEM/FIB workstation. A direct comparison with a laser-treated sample surface does not disclose any considerable difference in the positions of maximum laser intensity (see Fig. 6). Due to the relatively coarse grains, the resolidified microstructure is similar to the original one. This can be seen more clearly in a corresponding FIB cross section (Fig. 7).

Even in the positions of maximum laser intensity, the grain structure is not affected in an apparent way. Austenitic stainless steels are generally composed of the metastable $\gamma$-phase [23]. Thermal simulations were performed for the different structural wavelengths which have not shown any strong difference concerning the achievable temperatures in the positions of maximum and minimum intensity or the respective heating/cooling rates. Accordingly, the maximum temperature was approximately 1,900 K (in the maximum position) which is clearly above the corresponding melting range of the austenitic steel used ($T_m$ is between 1,693 and 1,747 K [24]).

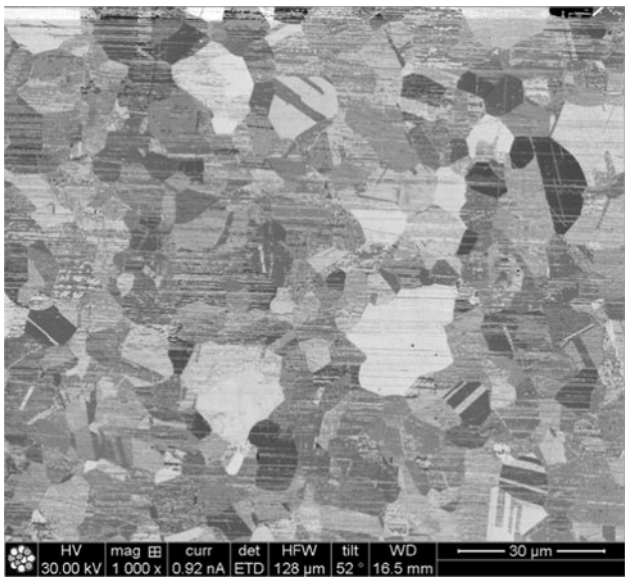


**Fig. 5** SEM/FIB image of the pristine steel surface. The image was recorded by means of ion channelling contrast

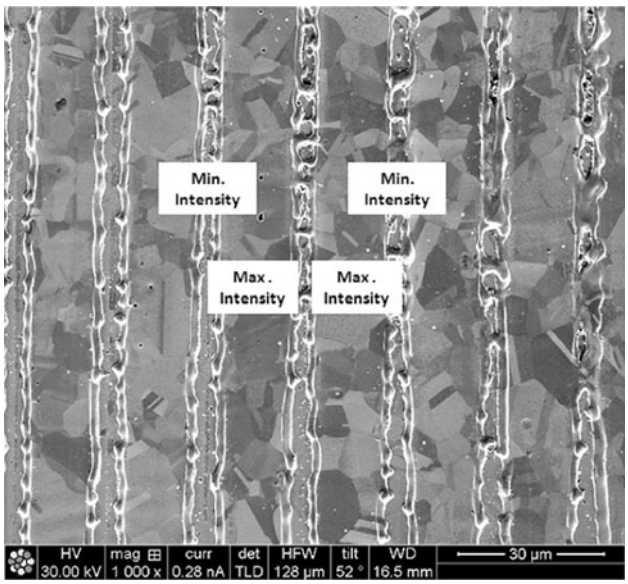


**Fig. 6** SEM/FIB image of the laser-treated steel surface which was recorded by means of ion channelling contrast. The laser intensity maxima correspond to the topographical minima with the clearly visible grain structure

In this context, X-ray diffraction was applied to study the effects of phase formation in the chosen steel before and after laser patterning. The corresponding diffractogram in Fig. 8 could be unambiguously identified and assigned to the austenitic phase in both cases. The structural wavelength of the laser-patterned sample was 18 µm in this case. Similar XRD results were found for 5 and 9 µm periodicities.

Furthermore, nanoindentation experiments were carried out in order to measure the hardness in the positions of maximum laser intensity and in the unpatterned reference

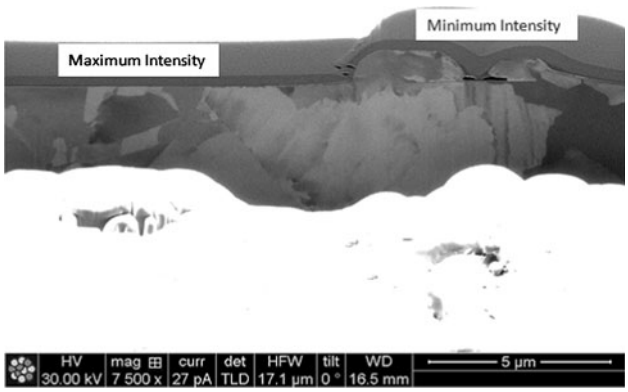


**Fig. 7** FIB cross section of a steel surface after laser patterning highlighting the grain morphology in the positions of maximum and minimum laser intensity. The *dark grey* layer on top of the sample surface represents a Pt protection layer resulting from the FIB cross section preparation and does not represent the oxide film

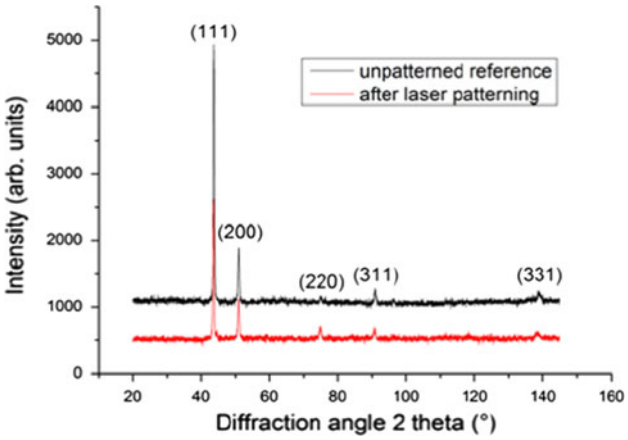


**Fig. 8** Grazing incidence X-ray diffractogram of the unpatterned and laser-treated steel sample. The structural wavelength was 18 µm in this case

regions. A Berkovich (three-sided pyramidal tip, 142.3°) diamond indenter was carefully calibrated for its area function on a standard testing material. The loading profile included three segments: loading to a 300 µN peak load within 5 s; holding at the peak load for 15 s; and unloading back to zero load in 5 s. No considerable thermal drift was observed during the measurements. The loading rate for all indents was set to 60 µN/s. Figure 9 shows the results of the hardness measurement for the polished reference and the laser-patterned surface. Here, only laser intensity maxima, representing the topographical minima, could be indented. Due to the melting process, the laser intensity minima are quite inhomogeneous and too narrow to be indented (see Fig. 6). Despite some data scatter, most of the values are similar and thus consistent with the previous SEM images. The average hardness value and standard deviation is $2.24 \pm 0.55$ GPa for the reference and

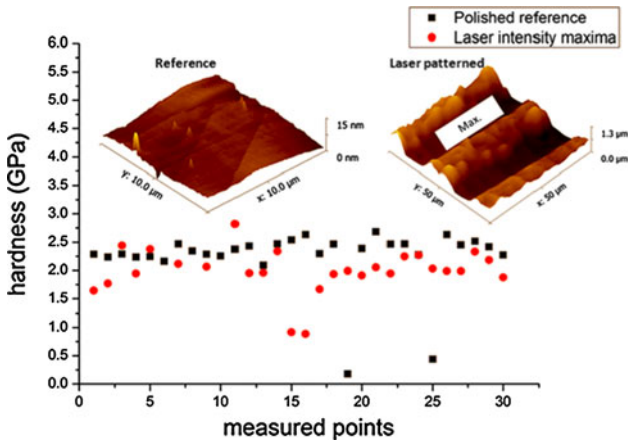


**Fig. 9** Measured hardness of the reference and laser-patterned specimen surfaces with corresponding 3-D surface plots recorded by a Hysitron tribo-indenter. Only measurement points for the laser intensity maxima positions (topographical minima) are displayed. The structural wavelength was 18 μm

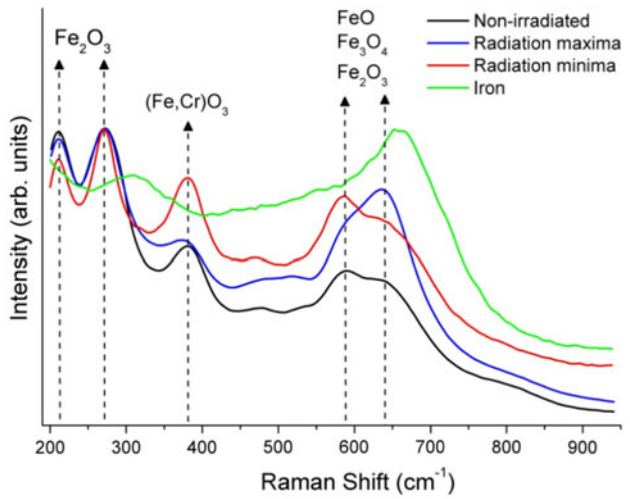


**Fig. 10** Raman spectra measured on different topographical zones identified in Fig. 6. The laser spot size was 5 μm and the information depth was ~1 μm measured from the samples surfaces. Differences between the spectra indicate that the laser pattering irradiation induced a different oxidation state of the surface. The structural wavelength was 18 μm

2.45 ± 0.62 GPa for the patterned specimen. In conclusion, no severe micro-mechanical changes could be detected by the methods used in this work. However, further high-resolution techniques will be necessary to study the microstructure more in detail.

### 3.3 Surface Chemistry

Raman analysis was carried out on the structured samples in order to study the chemical species present in different topographical zones. In order to obtain representative and reliable information, the analysis was performed ten times on each topographical zone identified in Fig. 6. As expected, similar species were found in the non-irradiated and irradiated areas (see Fig. 10). The low-frequency peaks located at around 210 and 270 $cm^{-1}$ correspond to vibrations of $Fe_2O_3$ observed in Fe–Cr–Ni alloys [25] and steel [26], whereas the peak located at ~380 $cm^{-1}$ was observed in (Fe, Cr)$O_3$ [27]. Moreover, the modes with wave numbers at around 590 and 640 $cm^{-1}$ have been observed in several materials containing FeO, $Fe_3O_4$ and $Fe_2O_3$ [28–31].

It is worth noting the change of the relative intensities of the peaks located at around 590 and 640 $cm^{-1}$. As expected, similar intensities with respect to the background are observed in the non-irradiated and minimum irradiated samples, whereas the intensity of the peak located at ~640 $cm^{-1}$ increased in the radiation maxima zones. Since the exact vibration of this mode is not clear in the literature [25–31], the interpretation of this observation is not straightforward. Besides FeO, this mode may have contributions from magnetite ($Fe_3O_4$), maghemite ($\gamma$-$Fe_2O_3$) and hematite ($\alpha$-$Fe_2O_3$), due to phase transformations induced by high-temperature processes [30, 31].

Moreover, as shown in Fig. 10, the peaks at ~270 and ~640 $cm^{-1}$ are shifted between the spectra of the 99.99 % pure iron and the radiation maxima zone, and the intensity/background ratio of the mode associated with (Fe, Cr)$O_3$ species decreased in the maximum radiation zone. The synergy of these evidences strongly indicates a modification of the oxidation state of the surface after laser patterning.

### 3.4 Tribological Results

Finally, the as-patterned surfaces were analysed in linear reciprocating sliding tests. In order to ensure stochastic significance and reproducibility, all tests were repeated at least ten times. In order to get a better understanding of the tribological kinematics and the relative alignment of the contacting bodies, Fig. 11a and b depict a 3-D view of the structured steel sample and tribometer ball. The sliding velocity was kept constant at 1 mm/s. The labelling 0°/90° denotes the angle between the linear structures and the black arrow indicates the sliding direction in our experiments. In addition, the friction coefficient $\mu$ as a function of sliding time for two different periodicities is shown in Fig. 11c and d. The curves displayed in Fig. 11c and d are averaged plots of the friction coefficient of forward and backward strokes. After having exceeded the initial static friction, $\mu$ for the polished reference surface is larger than for the patterned specimens, independent of the relative alignment (0°/90°) between the rubbing partners. A closer look at the orientation of the surfaces reveals that the results for the 5 and 18 μm structural wavelengths

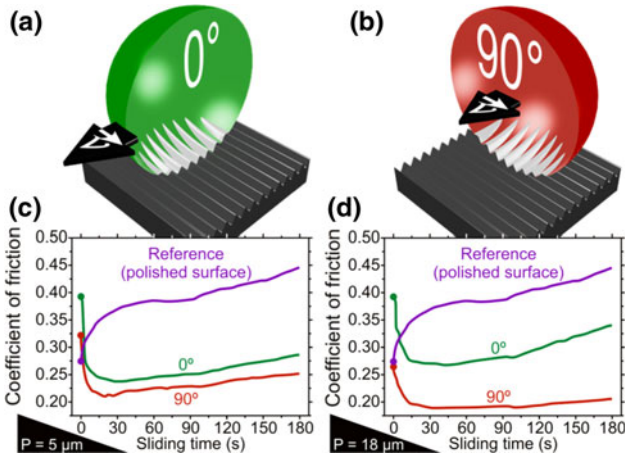


**Fig. 11** **a**, **b** Display a 3-D view of the relative alignment and sliding direction of the patterned contacting surfaces indicated by the *black arrows*. **c**, **d** Show the temporal evolution of $\mu$ for different alignments (0°/90°) and two periodicities (5 and 18 µm) compared to the unpatterned reference surface

demonstrate a lower $\mu$ for a 90° alignment although the (initial) surface chemistry and the microstructural properties are obviously independent of the relative orientation. Therefore, it can be concluded that this observation is consistent with a structural incompatibility compared to the 0° alignment and finally to a reduced contact area [32]. In the case of a 0° alignment, the initial value of $\mu$ after the laser treatment ($\mu \sim 0.4$) deviates from the reference value ($\mu \sim 0.27$) of the pristine surface, independent of the chosen structural wavelength. This might be explained by a potential interlocking at 0°, different surface chemistry and microstructural situation after the laser treatment (e.g. higher defect density). However, while interlocking automatically increases static friction, it does not necessarily explain an increased kinetic friction.

A closer look at the resulting wear scars for the two different sliding directions (0°/90°) is shown in Fig. 12. As expected in the case of 0° alignment, the wear track is more pronounced whereas for an angle of 90° only a slight wear scar can be identified.

A comparison of Fig. 11c and d further implies a strong effect of the different structural wavelengths.

The temporal evolution of $\mu$ for the 0° orientation is demonstrated in Fig. 13 for three different wavelengths (5, 9 and 18 µm). The coefficients of friction of all the laser-patterned specimens are initially higher than that of the pristine, unpatterned surface. The reference value starts at about 0.27 and increases with sliding time. This increase of $\mu$ over the sliding time can be divided into two parts with differing slopes indicating a change in the friction mechanism. Raman spectroscopy in combination with focused ion beam cross sections has revealed the existence of a native oxide layer in the reference material. The typical oxide layer thickness is in the range of $\sim$5 nm. Measurements of the oxide layer after the laser treatment by FIB cross sections have demonstrated much thicker oxide layers of approximately 26 nm thickness at the intensity maxima (topographical minima). Because of the inhomogeneous structure of the intensity minima (topographical maxima), no reliable thickness of the oxide layer could be determined in the cross section.

It is known from the literature that the steel–steel friction coefficient under dry and clean conditions is smaller in

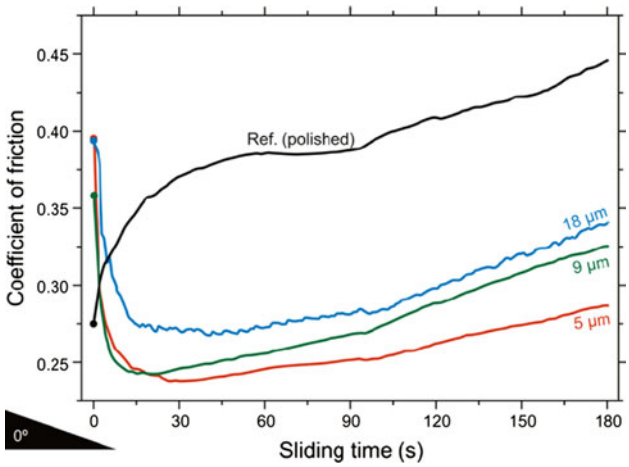


**Fig. 13** Coefficient of friction over sliding time for three distinct line-spacings at 0° orientation

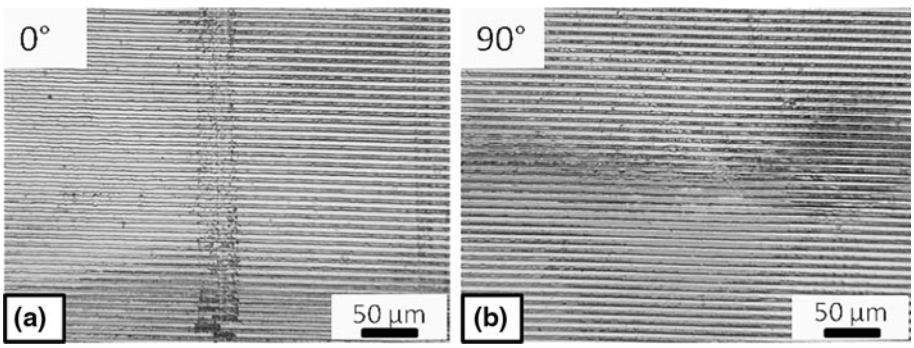


**Fig. 12** Light microscopy image of wear tracks with a 0° orientation between substrate and ball (**a**) and a 90° orientation (**b**)

the presence of these oxide layers (typically 0.27) than in their absence ($\mu \sim 0.80$) [33]. The friction coefficient of the reference in the beginning is in good agreement with the reported $\mu$ of 0.27.

The initial values of $\mu$ of the laser-patterned surfaces are approximately 30 % higher compared to the reference surface for a 0° orientation. This may be attributed to an interlocking effect as well as a modified chemical and microstructural state of the laser irradiated samples in which the composition of the oxide layers differs from the pristine material surface and the defect density (e.g. dislocations) may be increased. Subsequent to the initial situation, $\mu$ of the laser-patterned surfaces decreases independent of the used periodicity. An explanation for this decline after some run-in could be that the induced patterns gradually degrade, which can reduce the interlocking of asperities. The local properties of the patterned specimens become similar to those of the reference.

After the sudden drop of $\mu$, an increase can be observed which may be linked to further flattening of the laser structures causing a larger real contact area and a changed surface chemistry.

In Fig. 14, a direct comparison of the laser-induced surface profile is presented before and after sliding. The profile amplitude after sliding is visibly reduced and the profile looks more flattened after the sliding deformation.

Furthermore, after a sliding time of around 90 s, a deviating slope for all the specimens is visible. During sliding, oxide wear particles are created and shifted to the reversal points of the slider thus accumulating at the end of the wear track, as indicated by light microscopy. As a result, the friction regime is changed because the oxide layer is gradually removed and the friction coefficient approaches the reported value of 0.8 for the steel–steel contact without oxide layer. While the surface chemistry and surface topography certainly play important roles concerning the initial values and various slopes in the friction curves, they cannot explain the significant differences in $\mu$ for 0° and 90° orientation. One difference between the different orientations is their relative contact areas. They would yield different total friction assuming local friction-load relationships of the form $F_s = \sigma_0 A_{real} + \alpha_p L$. $F_s$ and $L$ denote the friction force and the normal load on a representative surface element, respectively, whereas the system-dependent $\sigma_0$ and $\alpha_p$ stand for an offset and a proportionality coefficient [1]. This constitutive relation holds all the way down to the nanometre scale in the presence of lubricants or contaminants, with values in the order of 0.1 leading to a reduced but not vanishing friction [34]. We will explore the possibility of contact area being important in a separate study.

As far as the wavelength dependency is concerned, we suppose on the one hand that this experimental result may be traced back to the mean square slopes of the measured profiles. The mean square slope $S_{RMS}$ shows a maximum value for a structural wavelength of 5 µm whereas the smallest $S_{RMS}$ can be found for 18 µm. This value is in leading order inversely proportional to the real contact area [35]. On the other hand, the observed friction reduction may also be a consequence of fabrication errors during the patterning process. The resulting laser patterns are not perfectly sinusoidal and thus the interlocking could be complicated for a 0° alignment and a decreasing structural wavelength.

In general, the tribological behaviour of austenitic stainless steels is strongly affected by the formation of strain-induced ε-martensite [36]. According to Huebner et al. [36], the martensitic transformation might occur by shear deformation of the lattice. During sliding, the dislocation density increases and, as a consequence, so does the stacking fault density. These steels have a relatively low stacking fault energy of about 18 mJ/cm$^2$ which is comparable to that of Ag [37].

As already discussed, the stacking fault energy has a significant impact on the mechanical behaviour [38]. Like ε-martensite, the formed stacking faults are of hexagonal symmetry and thus finally pile up to form ε-martensite [36].

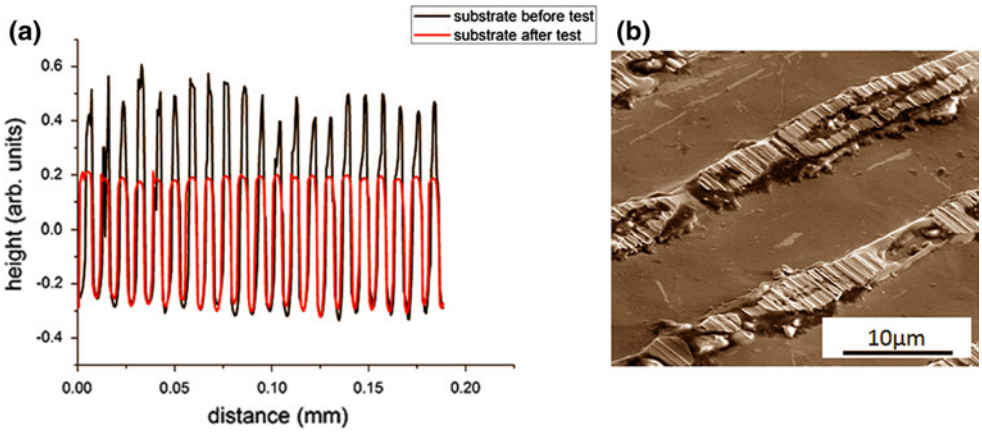


**Fig. 14** **a** Comparison of a laser-induced surface profile before and after sliding at a 0° orientation measured by WLI. **b** SEM image of the worn surface pattern under a tilt angle of 52°. The structural wavelength was 18 µm

Remarkable work in this field has also been published by Rigney and Hirth. Rigney [39] reported about the occurrence of large plastic strain fields during sliding deformation resulting in a strong rise of dislocations which organise themselves in dislocation cell structures. Typical values for dislocation densities after sliding contact of ductile metals are in the range of $10^{15}$ $1/m^2$ which is consistent with simulation results from Kuhlmann-Wilsdorf [39, 40]. X-ray diffraction could not prove the existence of martensite after laser irradiation. However, further experimental work is necessary to study the potential formation of martensite and the influence of dislocations and stacking faults on the friction behaviour of the steel used, before and after laser patterning as well as after the friction experiments by high-resolution techniques. In particular, TEM and XPS experiments are a current matter of subject for more detailed studies of the microstructural and depth-sensitive chemical situation.

## 4 Conclusions

In conclusion, we have found that the dry friction between two laser-structured solids depends not only on the wavelength of the structuring but also on the relative orientation between the patterns. Surface chemistry and mechanical properties, such as hardness and yield strength, can differ for different wavelengths and might be partly responsible for why different wavelengths produce different friction. However, considering their influence cannot explain the critical role of alignment: in each experiment, the friction for misaligned surfaces turned out smaller than for a perfectly oriented interface, given the same wavelengths in both experiments. One possibility for the origin of the dependence on alignment is that the contact area is alignment dependent. We explore this idea more in detail in a companion paper [41].

## References


1. Bowden, F.P., Tabor, D.: Mechanisms of metallic friction. Nature **150**, 197–199 (1942)
2. Hirano, M., Shinjo, K., Kaneko, R., Murata, Y.: Anisotropy of frictional forces in muscovite mica. Phys. Rev. Lett. **67**, 2642–2645 (1991)
3. Dienwiebel, M., et al.: Superlubricity of graphite. Phys. Rev. Lett. **62**(126101), 1–4 (2004)
4. Sondhauß, J., Fuchs, H., Schirmeisen, A.: Frictional properties of a mesoscopic contact with engineered surface roughness. Tribol. Lett. **42**, 319–324 (2011)
5. Urbakh, M., Klafter, J., Gourdon, D., Israelachvili, J.: The nonlinear nature of friction. Nature **430**, 525–528 (2004)
6. Willis, E.: Surface finish in relation to cylinder liners. Wear **109**, 351–366 (1986)
7. Gerbig, Y., Dumitru, G., Romano, V., Spassov, V., Haefke, H.: Effects of laser texturing on technical surfaces. MRS Proc. **750**, Y5.37 (2002)
8. Etsion, I., Kligerman, Y., Halperin, G.: Analytical and experimental investigation of laser-textured mechanical seal faces. Tribol. Trans. **42**, 511–516 (1999)
9. Pettersson, U., Jacobson, S.: Influence of surface texture on boundary lubricated sliding contacts. Tribol. Int. **36**, 857–864 (2003)
10. Rapoport, L., et al.: Wear life and adhesion of solid lubricant films on laser-textured steel surfaces. Wear **267**, 1203–1207 (2009)
11. Li, J., et al.: Effect of surface laser texture on friction properties of nickel-based composite. Tribol. Int. **43**, 1193–1199 (2010)
12. Kelly, M.K., et al.: High resolution thermal processing of semiconductors using pulsed-laser interference patterning. Phys. Stat. Sol. A **166**, 651–657 (1998)
13. Mücklich, F., et al.: Laser interference metallurgy-using interference as a tool for micro/nano structuring. Int. J. Mater. Res. **97**, 1337–1344 (2006)
14. Sun, Z., et al.: Two- and three-dimensional micro/nanostructure patterning of CdS—polymer nano composites with a laser interference technique and in situ synthesis. Nanotechnology **19**(3), 1–8 (2008)
15. Huang, J., et al.: Tunable surface texturing by polarization-controlled three-beam interference. J. Micromech. Microeng. **20**, 1–6 (2010)
16. Daniel, C., Mücklich, F.: Micro-structural characterization of laser interference irradiated Ni/Al multi-films. Appl. Surf. Sci. **242**, 140–146 (2005)
17. Nebel, C.E., et al.: Laser-interference crystallization of amorphous silicon—applications and properties. Phys. Stat. Sol. A **166**, 667–673 (1998)
18. Gachot, C., et al.: Comparative study of grain sizes and orientation in microstructured Au, Pt and W thin films designed by laser interference metallurgy. Appl. Surf. Sci. **255**, 5626–5632 (2009)
19. Gao, F., Leach, R., Petzing, J., Coupland, J.: Surface measurement errors using commercial scanning white light interferometers. Meas. Sci. Technol. **19**, 1–13 (2008)
20. Lasagni, A.F., D′Alessandria, M., Giovanelli, R., Mücklich, F.: Advanced design of periodical architectures in bulk metals by means of laser interference metallurgy. Appl. Surf. Sci. **254**, 930–936 (2007)
21. Lasagni, A.F.: Advanced design of periodical structures by laser interference metallurgy in the micro/nano scale on macroscopic areas. PhD thesis, Saarland University, Saarbrücken (2006)
22. Carbone, G., Bottiglione, F.: Asperity contact theories—do they predict linearity between contact area and load. J. Mech. Phys. Solids **56**, 2555–2572 (2008)
23. Talonen, J., Nenonen, P., Pape, G., Hänninen, H.: Effect of strain rate on the strain- induced $\gamma \rightarrow \alpha'$-martensite transformation and mechanical properties of austenitic stainless steels. Metall. Mater. Trans. A **36A**, 421–432 (2005)
24. Haynes, W.M., Lyde, D.R.: Handbook of Chemistry and Physics. CRC Press, Taylor and Francis Group, Boca Raton (2010)
25. Renusch, D., Veal, B., Natesan, K., Grimsditch, M.: Transient oxidation in Fe–Cr–Ni alloys—a Raman-scattering study. Oxid. Met. **46**, 365–381 (1996)
26. Oh, S.J., Cook, D.C., Townsend, H.E.: Characterization of iron oxides commonly formed as corrosion products on steel. Hyperfine Interact. **112**, 59–66 (1998)
27. McCarty, K.F., Boehme, D.R.: A Raman study of the systems $Fe_3$–$xCrxO_4$ and $Fe_2$–$xCrxO_3$. J. Solid State Chem. **79**, 19–27 (1989)

28. Farrow, R.L., Benner, R.E., Nagelberg, A.S., Mattern, P.L.: Characterization of surface oxides by Raman spectroscopy. Thin Solid Films **73**, 353–358 (1980)
29. Raman, R.K.S., Gleeson, B., Young, D.J.: Laser Raman spectroscopy—a technique for rapid characterisation of oxide scale layers. Mater. Sci. Technol. **14**, 373–376 (2011)
30. Odziemkowski, M.S., Schuhmacher, T.T., Gillham, R.W., Reardon, E.J.: Mechanism of oxide film formation on iron in simulating groundwater solutions: Raman spectroscopic studies. Corros. Sci. **40**, 371–389 (1998)
31. De Faria, D.L.A., De Oliveira, M.T.: Raman microspectroscopy of some iron oxides and oxyhydroxides. J. Raman Spectrosc. **28**, 873–878 (1997)
32. Müser, M.H.: Der mikroskopische Ursprung der Reibung. Phys. J. **2**, 43–48 (2003)
33. Campbell, W.E. Proceedings of M.I.T., p. 197. MIT Press, Cambridge (1940)
34. He, G., Robbins, M.O., Müser, M.H.: Adsorbed layers and the origin of static friction. Science **284**, 1650–1652 (1999)
35. Persson, B.N.J.: Theory of rubber friction and contact mechanics. J. Chem. Phys. **115**, 3840–3861 (2001)
36. Hübner, W.: Phase transformations in austenitic stainless steels during low temperature tribological stressing. Tribol. Int. **34**, 231–236 (2001)
37. Schramm, R.E., Reed, R.P.: Stacking fault energy of seven commercial austenitic stainless steels. Metall. Mater. Trans. A **6A**, 1345–1351 (1975)
38. Feller, H.G., Gao, B.: Correlation of tribological and metal physics data: the role of stacking fault energy. Wear **132**, 1–7 (1989)
39. Rigney, D.A.: Large strains associated with sliding contact of metals. Mater. Res. Innov. **1**, 231–234 (1998)
40. Kuhlmann-Wilsdorf, D.: Dislocation behavior in fatigue IV. Quantitative interpretation of friction stress and back stress derived from hysteresis loops. Mater. Sci. Eng. **39**, 231–245 (1979)
41. Prodanov, N., Gachot, C., Rosenkranz, A., Mücklich, F., Müser, M.H.: Contact mechanics of laser-textured surfaces—correlating contact area and friction. Tribol Lett. doi:10.1007/s11249-012-0064-z